

Effects of spatial autocorrelation structure for friction angle on the runout distance in heterogeneous sand collapse

Guotao Ma¹, Mohammad Rezaia², Mohaddeseh Mousavi Nezhad³

Abstract

This paper proposes a stochastic method for analyzing the runout distance of sand collapse considering the spatial variability of shear strength, in which random field theory and generalized interpolation material point method are integrated into a Monte-Carlo simulation basis. The random field is generated by Cholesky matrix decomposition method and implemented into the material point level, hence heterogeneity and large deformations are simultaneously considered in the modeling process. A sand collapse case is simulated with both homogeneous and heterogeneous condition assumptions by the proposed method. The effect of five theoretical autocorrelation functions (ACFs) on the runout distance of the collapse is highlighted since the ACFs are commonly adopted to characterize the spatial variability of soil properties due to sparse site observation data. It is shown that the deterministic analysis may underestimate the runout distance, while the heterogeneous model provides realistic results. Moreover, five ACFs and

¹Research Assistant, School of Engineering, University of Warwick, Coventry, UK.

Email: g.ma.1@warwick.ac.uk. ORCID: <https://orcid.org/0000-0001-9783-413X>

²Reader, School of Engineering, University of Warwick, Coventry, UK. (Corresponding Author)

Email: m.rezania@warwick.ac.uk. ORCID: <https://orcid.org/0000-0003-3851-2442>

³Reader, School of Engineering, University of Warwick, Coventry, UK.

Email: m.mousavi-nezhad@warwick.ac.uk. ORCID: <https://orcid.org/0000-0002-0625-439X>

different coefficients of variation of friction angle (COV_{φ}) are compared to investigate their influences on the runout distance modeling. The results show that the uncertainty of runout distance increases with the increase in COV_{φ} . Meanwhile, the variances of the runout distance also become larger with COV_{φ} increasing. Based on the proportion of the runout distance which exceeds the deterministic value, the results indicate that the deterministic analysis notably underestimates the risk induced by large runout distances in real heterogeneous granular flows (e.g., landslide, debris-avalanches).

Author Keywords: Random field, Sand collapse, Runout distance, Spatial variability.

1. Introduction

In nature, the flow of granular material is a common phenomenon in geological disasters such as landslides, debris flows, and avalanches (Crosta et al., 2009; Ma et al., 2018). Therefore, landslides are often treated as granular flows with diverse behaviors ranging from solid-like to fluid-like. Landslides as a real geophysical flow are primarily driven by gravity and could result in catastrophic damages along their extensive motion paths, such as destroying transportation infrastructures, facilities, and buildings (Huang and Fan, 2013). Especially, all transportation in mountainous regions face great challenges given their exposure to long runout distance and huge influence zone of potential landslides (Yerro et al., 2019; Wang et al., 2020). Additionally, this is further complicated due to the spatial variability of the geomaterials involved, with natural heterogeneity in these flows. Therefore, for risk assessment and disaster mitigation, prediction of the final extent of granular flow in spatially varying deposits is crucial to precisely investigate the post-failure behavior, which plays a significant role in real landslides.

Collapse of a granular column has been extensively studied in the case of dry granular material (Fern and Soga, 2017). Lube et al. (2004) and Lajeunesse et al. (2004) are the first to conduct the experiments by releasing a column of granular material on a flat surface to investigate the flow mechanisms and geometrical properties of the final deposits. Since then, granular flows are also investigated using several numerical approaches such as discrete element method (DEM) (Guo and Curtis, 2015), smooth particle hydrodynamics (SPH) (Bui et al., 2008; Nguyen et al., 2017), and material point method (MPM) (Li et al., 2018) which compensated the details of granular flows on stress-strain and final runout distance by different aspect ratios and mechanical parameter settings. Among the mentioned methods, DEM is deemed to be an accurate approach to simulate granular flows, but it requires demanding computational resources for a practical problem involving hundreds of millions of particles. In addition, the difficulty in selection of appropriate micro-parameters is a main drawback in DEM, particularly for practical level simulations (Benvenuti et al., 2016). As for particle-based method, inconsistent near boundaries (Morris, 1996) and tensile instability (Bui et al., 2008) would result in low accuracy and greatly limit the application of SPH in geo-engineering. This leads to the increasing development and application of MPM in modeling granular flow problems (Bardenhagen et al., 2000; Iaconeta et al., 2017; Li et al., 2018). However, in previous studies the granular materials are always assumed to be homogeneous and modeled with simplified homogeneous and isotropic material models without considering the spatial variability and uncertainty of their heterogeneity. Meanwhile, it is impractical to conduct hundreds of physical experiments to investigate the runout distance affected by natural heterogeneities in different geomaterial deposits. However, in engineering geology, variability of natural geomaterials (e.g., sand, silt, clay) is extensively admitted, and it is agreed that the spatial distributions of shear strength parameters (e.g., internal friction angle φ and

cohesion c) notably influence the likelihood and failure mode of these flows, thereby influencing their post-failure behavior and runout motion. Kerswell (2005) indicated that the runout behavior of granular flows has a clear material dependence, even little variability in material strength could result in a totally different response. According to Crosta et al. (2009) and Zhang and Xiao (2019) the internal friction angle plays a particularly important role on the post-failure behavior of granular flows. However, currently conventional deterministic particle-based methods cannot investigate the effect of spatial variability of shear strength parameters on runout motion. Therefore, analyzing runout distance of the granular flow in spatially varying soils is still an open question.

In recent decades, many probabilistic studies have been conducted as the complementation for deterministic analysis in geotechnical engineering. Spatial variability of soil properties is commonly considered as weakly stationary random fields (Fenton and Griffiths, 2003; Griffiths and Fenton, 2004; Jiang et al., 2014), which is based on random field theory (Vanmarcke, 1977; Nezhad, 2010; Nezhad et al., 2011). In the previous studies, the spatially varying shear strength is usually modeled as a random variable in a structural correlation computational domain (Liu, 2018; Zhang et al., 2018; Gironacci et al., 2018; Nezhad et al., 2018), and the stability/reliability of geo-structures (e.g., foundation or slope) and corresponding probability of failure is evaluated by limit equilibrium method (LEM), finite element method (FEM), or finite difference method (FDM). Among these studies, it can also be noticed that they have been mainly focused on failure probability or pre-failure phase and do not consider the effect of spatial variability on large deformation problems or moving behaviors at post-failure phase. Consequently, post-failure analysis of heterogeneous granular flows is predominantly overlooked in previous works, hence its resulting consequences from the extensive runout of deposits under the effect of inherent spatial

variability were also largely ignored. Part of the reason is that large deformation and strain alternation in the computation domain at post-failure phase cannot be easily simulated and analyzed by LEM and FEM methods (e.g., due to mesh dependency, mesh distortion or twisting problems). On the other hand, the lack of such research is partly because of the difficulty in implementing random field information into the modeling framework in an efficient way.

In this paper, a generalized interpolation MPM (GIMP) based stochastic numerical modeling framework, termed SGIMP, is employed for simulating granular column collapse in heterogeneous sands with the aim to investigate the spatial variability of shear strength with different autocorrelation functions (ACFs) on the runout distance. The method utilizes both advantages of GIMP and random field theory. According to Crosta et al. (2009), Mohr-Coulomb constitutive model is suitable for capturing the dynamics of collapse in non-cohesive deposits, therefore the whole failure process is modeled by the SGIMP using this constitutive model. Given the large influence of internal friction angle on post-failure behavior (Zhang and Xiao, 2019), it is selected as the random variable and introduced by random field principle. A homogeneous sand collapse and a heterogeneous sand collapse are studied to demonstrate the validity of the method and explore the effects of ACFs and coefficient of variations (COVs) for the internal friction angle parameter. The results of this study can provide a new methodology and insight towards the enforcement of risk assessments for real landslides and other geomaterial flows.

2. Stochastic generalized interpolation material point method

2.1 Brief review of MPM

MPM was originally developed based on the strengths of particle-in-cell scheme (Sulsky et al., 1994) and FEM. It has been proven as a promising particle-based mesh free method in geotechnical

engineering for simulating large strain boundary value problems. The method has been applied to simulate granular flows, slope failures, landslides, embankment collapse and other geological and geotechnical problems (e.g., Andersen and Andersen, 2010; Llano-Serna et al., 2016; Li et al., 2018; Yerro et al., 2019). The essential idea in MPM is to take the advantages of both Lagrangian and Eulerian methods. A cluster of material points (Lagrangian points) is considered representing the continuous material and is allowed to freely move, carrying density, strain, stress, and all state variables of the continuous body; and a Eulerian background mesh is adopted for solving the governing equations of motion and determining incremental velocities, instead of carrying permanent information. In the convection phase, the updated information of grid nodes is mapped back to the material points, and subsequently the grid is regularly reset to the initial configuration and the deformation of the domain is tracked by the motion of the material points. As shown in a computational cycle (Fig. 1), the material points carrying information and background mesh are used to solve motion equations, update the material points, and refresh.

In a material domain Ω , it yields the mass and momentum conservation as follows:

$$\frac{d\rho}{dt} + \rho \nabla \mathbf{v} = 0 \quad (1)$$

$$\rho \frac{d\mathbf{v}}{dt} = \nabla \sigma + \rho \mathbf{b} \quad (2)$$

where, ρ is the mass density, \mathbf{v} is the velocity of material, σ is the *Cauchy* stress tensor, \mathbf{b} is the body force, and ∇ is the gradient operator.

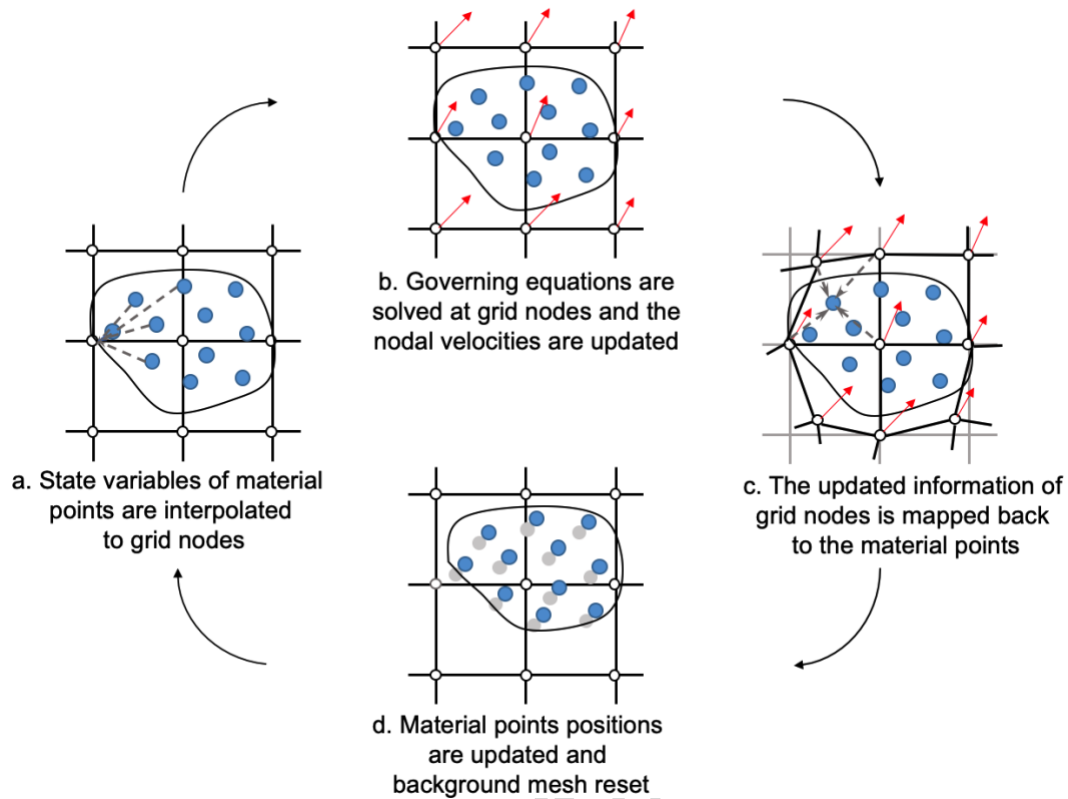


Fig. 1 The basic computational cycle in material point method

2.2 Generalized interpolation material point method

The original MPM has grid-crossing instability, which is caused by the discontinuous gradient of shape functions (Bardenhagen et. al., 2002). A sudden change of the stress can be found when a material point crosses to a new cell. This error can be reduced by using GIMP method to introduce GIMP grid shape function and particle characteristic function (Bardenhagen and Kober, 2004). This paper uses GIMP as implemented in the open-source code named MPM3D, from the Computational Dynamics Laboratory, School of Aerospace, Tsinghua University (Zhang et al., 2016). The main computational cycle of GIMP is summarized in the following four steps:

1. Firstly, state variables of material points (e.g., mass, momenta, etc.) are interpolated to grid nodes on the mesh, the mass of a node i and nodal momentum is expressed as:

$$m_i = \sum_{p=1}^n S_{ip} m_p \quad (3)$$

$$p_i = \sum_{p=1}^n S_{ip} m_p v_p \quad (4)$$

where S_{ip} is the computational grid shape function of node i for particle p in GIMP, m_p is the mass, v_p is the velocity.

2. Then the nodal internal force f_i^{int} and external force f_i^{ext} at the node i are expressed as:

$$f_i^{int} = - \sum_p \nabla S_{ip} \sigma_p V_p \quad (5)$$

$$f_i^{ext} = \sum_p S_{ip} b_p m_p \quad (6)$$

where ∇S_{ip} is the gradient of the computational grid shape function over the particle p , σ_p is the *Cauchy* stress at the particle p , V_p is the volume of the particle, b_p is the corresponding body force. Based on the forces, the nodal velocities can be updated from:

$$v_i^{n+1} = v_i^n + \frac{f_i^{int} + f_i^{ext}}{m_i} \Delta t \quad (7)$$

3. The velocity of the particle p can be computed from the updated nodal velocity:

$$v_p^{n+1} = v_p^n + \sum_i S_{ip} \frac{f_i^{int} + f_i^{ext}}{m_i} \Delta t \quad (8)$$

4. The position of the particle is then updated:

$$x_p^{n+1} = x_p^n + \sum_i S_{ip} v_i^{n+1} \Delta t \quad (9)$$

Finally, the background mesh is discarded and refreshed to undistorted configuration. Note that the above computational cycle can be repeated for each incremental step Δt . The used GIMP code is modified from the openly available MPM3D code (Zhang et al., 2016), which has been previously exercised by other researchers (e.g., Li et al. 2018).

2.3 Random field generation

Inherent spatial variability of soil is commonly represented by a numerically generated random field, which is based on first and second moments of variables and spatial correlation structure function. To generate a random field of a domain Ω , assume the domain is discretized into n elements with the centroid coordinates (x_i, y_i) , the autocorrelation matrix $\mathbf{C}_{n \times n}$ defining spatial structure of the domain can be expressed by:

$$\mathbf{C}_{n \times n} = \begin{bmatrix} 1 & \rho(\tau_{x_{12}}, \tau_{y_{12}}) & \dots & \rho(\tau_{x_{1n}}, \tau_{y_{1n}}) \\ \rho(\tau_{x_{21}}, \tau_{y_{21}}) & 1 & \dots & \rho(\tau_{x_{2n}}, \tau_{y_{2n}}) \\ \vdots & \vdots & \ddots & \vdots \\ \rho(\tau_{x_{n1}}, \tau_{y_{n1}}) & \rho(\tau_{x_{n2}}, \tau_{y_{n2}}) & \dots & 1 \end{bmatrix} \quad (10)$$

where, n represents the number of random field elements, $\rho(x_{ij}, y_{ij})$ is the autocorrelation coefficient of quantities between two spatial locations, τ is the absolute distances between the

centroid coordinates of the i th element and j th element in horizontal and vertical directions, respectively.

Generally, the correlation of any two variables at different locations is usually characterized by an ACF in a random field. As reported in the literature, DeGroot and Baecher (1993) adopted the maximum likelihood method to estimate the corresponding ACF of soil shear strength, Phoon and Ching (2014) tried to estimate the ACF by using moments method. However, determination of an appropriate ACF for soil properties is particularly difficult in practice because of limited site investigation, which requires extensive effort to obtain large quantities of geo-statistical data. Therefore, theoretical ACFs as alternatives are commonly used to characterize the spatial variability of soil properties (e.g., Phoon et al., 2003; Li et al., 2015; Liu, 2018). Based on the findings of previous studies carried out in the probabilistic analysis field, the five most commonly used theoretical ACFs for geo-statistical analysis can be pointed as; single exponential (SNX), widely used model to simulate inherent spatial variability of shear strength parameters (Griffiths and Fenton, 2004; Li et al., 2015), squared exponential (SQX), also named as Gaussian autocorrelation (Masoudian et al., 2019), cosine exponential (CSX) (Cafaro and Cherubini, 2002; Liu et al., 2017), second-order Markov (SMK) (Liu et al., 2017; Ching et al., 2019), and Binary noise (BIN) (Liu et al., 2017; Huang et al., 2018). Table 1 summarizes these five theoretical ACFs.

Table 1. Common ACFs for geostatistical analysis

Type	ACF in 1-D	Scale of fluctuation	ACF in 2-D
SNX	$\rho(\tau) = \exp(-a\tau)$	$\delta = 2/a$	$\rho(\tau_x, \tau_y) = \exp\left[-2\left(\frac{\tau_x}{\delta_h} + \frac{\tau_y}{\delta_v}\right)\right]$
SQX	$\rho(\tau) = \exp\left[-(b\tau)^2\right]$	$\delta = \sqrt{\pi}b$	$\rho(\tau_x, \tau_y) = \exp\left[-\pi\left(\frac{\tau_x^2}{\delta_h^2} + \frac{\tau_y^2}{\delta_v^2}\right)\right]$

SMK	$\rho(\tau) = \exp(-c\tau)(1 + c\tau)$	$\delta = 4/c$	$\rho(\tau_x, \tau_y) = \exp\left[-4\left(\frac{\tau_x}{\delta_h} + \frac{\tau_y}{\delta_v}\right)\right]\left(1 + \frac{4\tau_x}{\delta_h}\right)\left(1 + \frac{4\tau_y}{\delta_v}\right)$
CSK	$\rho(\tau) = \exp(-d\tau)\cos(d\tau)$	$\delta = 1/d$	$\rho(\tau_x, \tau_y) = \exp\left[-\left(\frac{\tau_x}{\delta_h} + \frac{\tau_y}{\delta_v}\right)\right]\cos\left(\frac{\tau_x}{\delta_h}\right)\cos\left(\frac{\tau_y}{\delta_v}\right)$
BIN	$\rho(\tau) = \begin{cases} 1 - e\tau & \text{for } \tau \leq 1/e \\ 0 & \text{otherwise} \end{cases}$	$\delta = 1/e$	$\rho(\tau_x, \tau_y) = \begin{cases} (1 - \frac{\tau_x}{\delta_h})(1 - \frac{\tau_y}{\delta_v}) & \text{for } \tau_x \leq \delta_h \text{ and } \tau_y \leq \delta_v \\ 0 & \text{otherwise} \end{cases}$

*The a, b, c, d, e are the scale of fluctuation parameters of the ACF model; the lags $\tau_x = |x_i - x_j|$ and $\tau_y = |y_i - y_j|$ are the absolute distances between two spatial locations in horizontal and vertical directions, respectively; δ_h and δ_v are the scale of fluctuation in horizontal and vertical directions, respectively.

For distinguishing the differences among the ACFs, the 2-D line graph and the 3-D surfaces of the ACFs are plotted in Fig. 2 and Fig. 3, respectively. It can be found that with the increasing of normalized absolute distance $|\tau|/\delta$, the corresponding autocorrelation coefficients associated with ACFs are very different. Meanwhile, significant differences can be observed among these surfaces of the ACFs, where $\rho(\tau_x, \tau_y)$ is the dependent variable, and τ_x and τ_y are the corresponding independent variables in horizontal and vertical directions, respectively. As Fig. 3 shows, among the surfaces, SNX decreases sharply with the increasing of τ_x and τ_y . The surfaces of SNX, CSX, and BIN ACFs exhibit a sharp corner near the origin and four edges, which are not differentiable. While the surfaces of SMK and SQX ACFs are very smooth and isotropic, which means the ACFs are differentiable at the origin. These five ACFs are used in this work to feature the spatial variability structure of shear strength in the computation domain and are utilized to investigate how the outputs change with various ACF conditions.

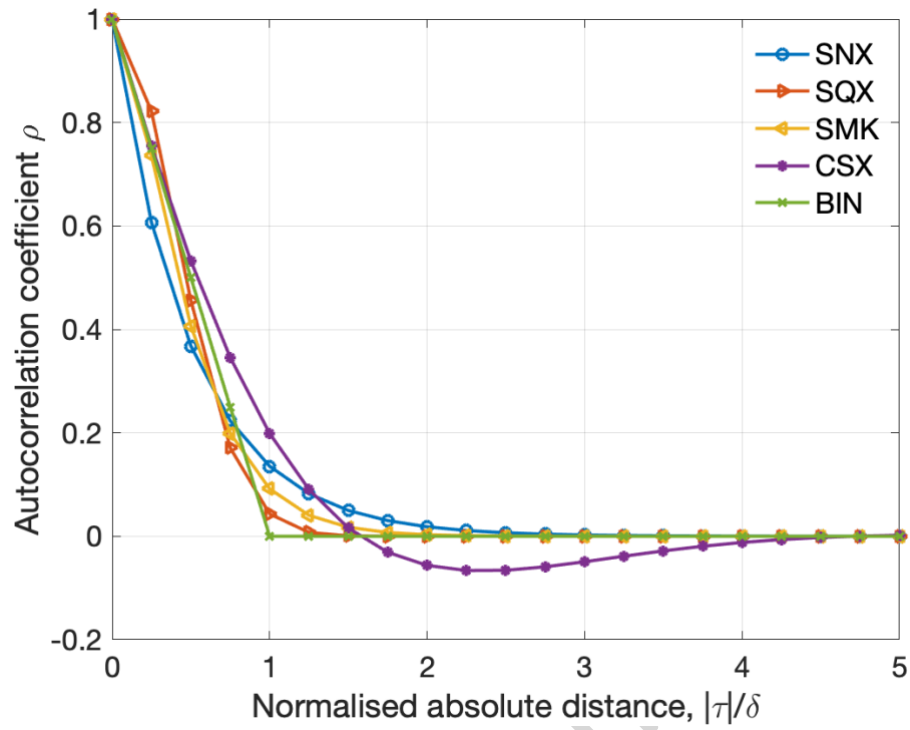
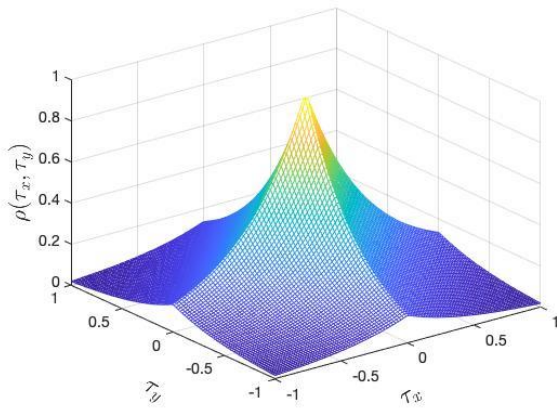
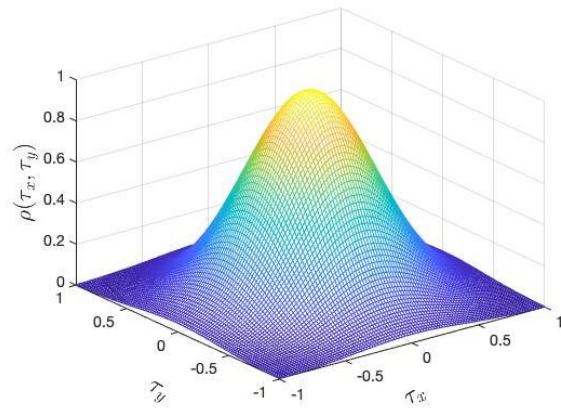


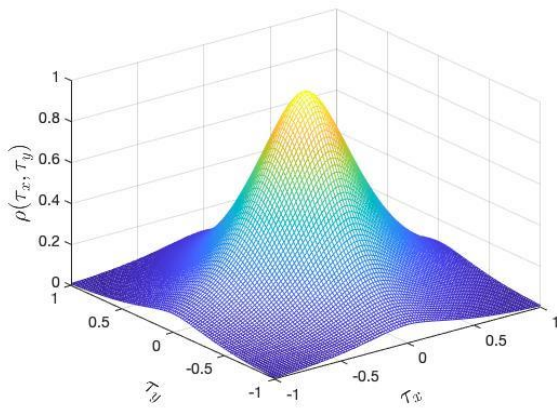
Fig. 2 Common ACFs for geostatistical analysis (normalized to unit scale of fluctuation)



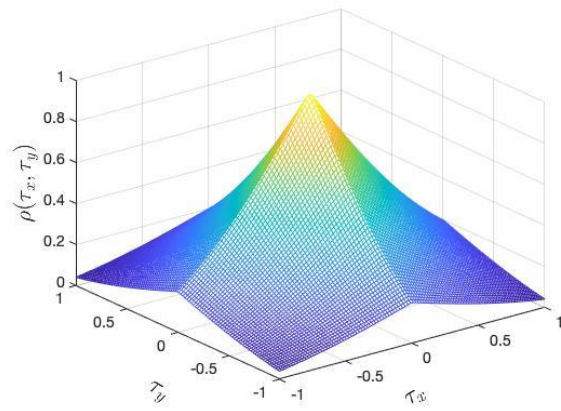
(a) SNX



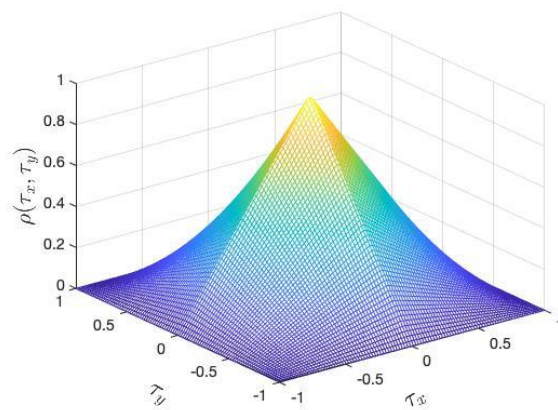
(b) SQX



(c) SMK



(d) CSX



(e) BIN

Fig. 3 3-D surfaces of the ACFs for geo-statistical analysis

2.3.1. Cholesky Matrix Decomposition Method

The Cholesky matrix decomposition (CMD) method (Li et al., 2015; Liu, 2018; Masoudian et al., 2019) is adopted in this paper to generate random fields. Karhunen-Loève expansion method can also be used for the same purpose; however, its application can result in a complex process as the eigenvalue of Fredholm integral equation could not be analytically readily solved (Zhu et al., 2017). CDM is computationally very efficient and easily implementable, it is also very robustly coping with multivariate random fields (Phoon et al., 2003; Phoon and Ching, 2014; Li et al., 2015). More details about generating random fields by using CMD can be found in Zhu et al. (2017). By using CMD, the autocorrelation matrix $\mathbf{C}_{n \times n}$ can be decomposed as:

$$\begin{aligned} \mathbf{C}_{n \times n} &= \mathbf{L} \cdot \mathbf{L}^T \\ &= \begin{bmatrix} 1 & 0 & \dots \\ \rho & \sqrt{1-\rho^2} & \dots \\ \vdots & \vdots & \ddots \end{bmatrix} \begin{bmatrix} 1 & \rho & \dots \\ 0 & \sqrt{1-\rho^2} & \dots \\ \vdots & \vdots & \ddots \end{bmatrix} \end{aligned} \quad (11)$$

where, \mathbf{L} is the lower triangular matrix with dimension of $n \times n$. An anisotropic standard Gaussian random field \mathbf{X}^G can be derived as follows:

$$\mathbf{X}^G(x, y) = \mathbf{L} \cdot \xi_i \quad (i = 1, 2, \dots, N) \quad (12)$$

where i is the number of standard Gaussian random field, ξ_i is a sample matrix obtained by arranging the vector of n independent standard normal random variables as m vectors with dimension of n . Subsequently, the standard Gaussian random field \mathbf{X}^G is used to generate the Non-Gaussian random field \mathbf{X}^{NG} of desired values by isoprobabilistic transformation method (Li et al., 2015) as:

$$\mathbf{X}^{NG}(x, y) = F^{-1}\Phi[\mathbf{X}^G(x, y)] \quad (i = 1, 2, \dots, N) \quad (13)$$

where the $F^{-1}(\bullet)$ is the inverse function of its corresponding marginal cumulative distribution of the desired variable given its mean μ , standard deviation σ , and probability distribution; $\Phi(\bullet)$ is the standard Gaussian cumulative distribution function. The $\Phi(\bullet)$ can rearrange the standard Gaussian random field \mathbf{X}^G into the uniform distribution $\mathbf{U} = \Phi[\mathbf{X}^G(x, y)]$ within (0,1). Thereafter, non-Gaussian random field \mathbf{X}^{NG} can be generated by Eq. (13), the procedure can be repeated N times to obtain N realisations of the random field.

2.4. Implementation and workflow of the framework

Fig. 4 outlines the basics of the SGIMP framework employed in this work, which consists of three important steps:

Step 1. In the pre-process phase, the random variable \mathbf{X} is set up based on the point statistics (mean μ_X , variance σ_X , and assumed distribution type, e.g., normal distribution), and the modules are initialized.

Step 2. In the SGIMP, Monte-Carlo simulation (MCS) is implemented for the stochastic modeling.

After setting the total realization number N , the current simulation starts from $i = 1$. Based on a set of random seed numbers, \mathbf{s} , the coordinates (x, y) of model geometry including the boundary conditions Γ , spatial structure defined by ACFs, and spatial statistics (scale of fluctuation δ), a set of isotropic Gaussian random fields $\mathbf{X}^G(x, y)$ can be generated. Then, it is transformed into the non-Gaussian random field $\mathbf{X}^{NG}(x, y)$ in the physical space by Eq. (13). It can be observed that all random fields may look similar in pattern; however,

they differ with respect to the spatial distribution of mechanically strong and weak zones that will lead to different output responses. The i -th set of spatially correlated soil property values $X^{NG}(x, y)$ is then transmitted to the mechanical module, which has been developed to perform the large deformation analysis. Meanwhile, a single set of deterministic model parameters \mathbf{D} (e.g., density ρ , Young's modulus E , Poisson's ratio ν) is transmitted to the mechanical module. After both deterministic model parameters and stochastic model parameters are prepared, the mechanical module starts to run the modeling and receives back a discrete response measure, runout distance $y = S_x$. This communication continues for N times realizations and until convergence of the first and second moments of the model outputs occurs. Here, it is assumed that the convergence occurs when the differences in the calculated values for mean and variance obtained in consequent MC iterations become less than 10^{-3} .

In the mechanical module, the most significant work about transmission of random fields to the mechanical module are highlighted. After running a MATLAB code of CMD method, the obtained i -th non-Gaussian random field $X^{NG}(x, y)$ of computation domain Ω holding the shear strength parameters of the geomaterial (in here the internal friction angle φ of sand) are mapped onto each material point in the GIMP instead of grid nodes as shown in Fig. 5. The transmission process is based on spatial relationship between material point and random field element (e.g., a position-to-position mapping process), which is similar with the RFEM sharing the same value on elements of random fields and FEM mesh (Huang and Griffiths, 2015).

Therefore, a deterministic GIMP calculation is performed after carrying a set of random mechanical property values on the material points. Consequently, stochastic modeling is conducted

and the output runout distance S_x is determined for each realization, i.e., $S_x = \{S_{x_1}, S_{x_2}, \dots, S_{x_n}\}^T$.

It should be noted that each simulation index, i , would be updated and checked; if $i \leq N$ the MCS is aborted, otherwise it is continued.

Step 3. In the post-processing phase, all calculated data are processed to compute the mean values, variances, and PDFs, and they will be compared with the corresponding homogeneous model outputs to investigate the effect of spatial variability on the runout distances. This framework can be easily extended to account for the uncertainty in other shear strength parameters of the deposit, such as undrained shear strength S_u , and any geometry. Furthermore, the outcomes can be used to assess and mitigate the potential damages incurred by large deformations during geo-disasters.

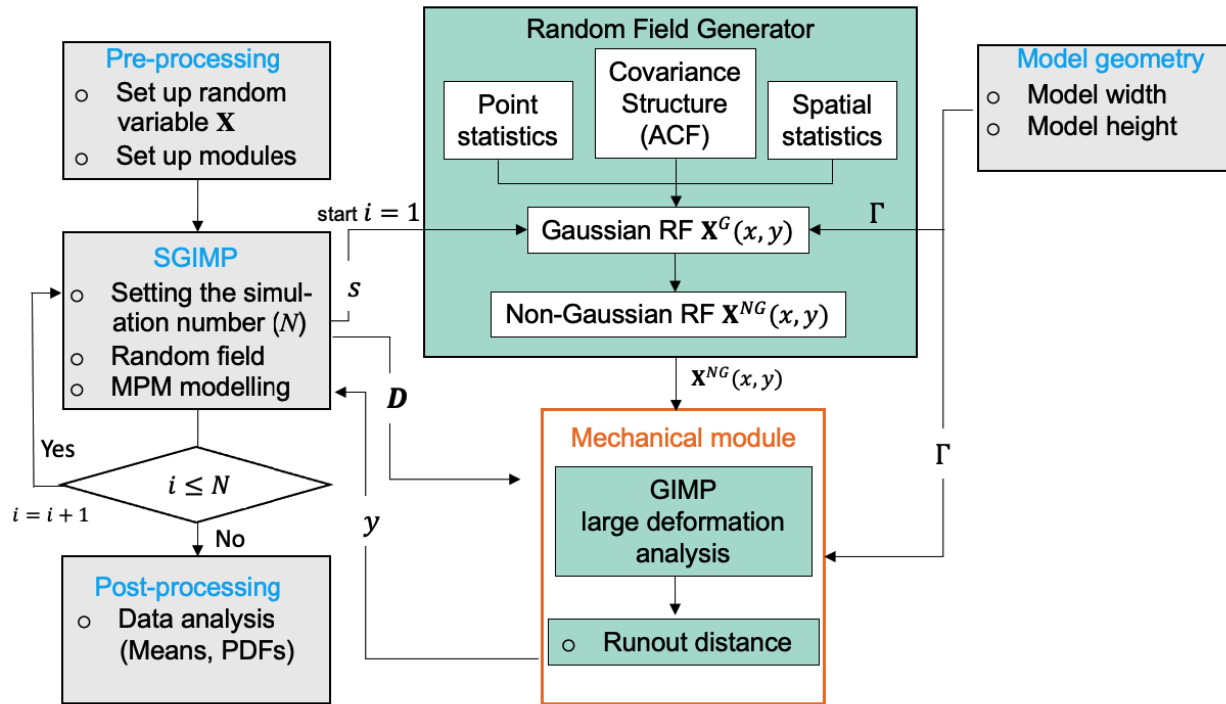


Fig. 4 Flowchart illustrating the employed SGIMP model framework

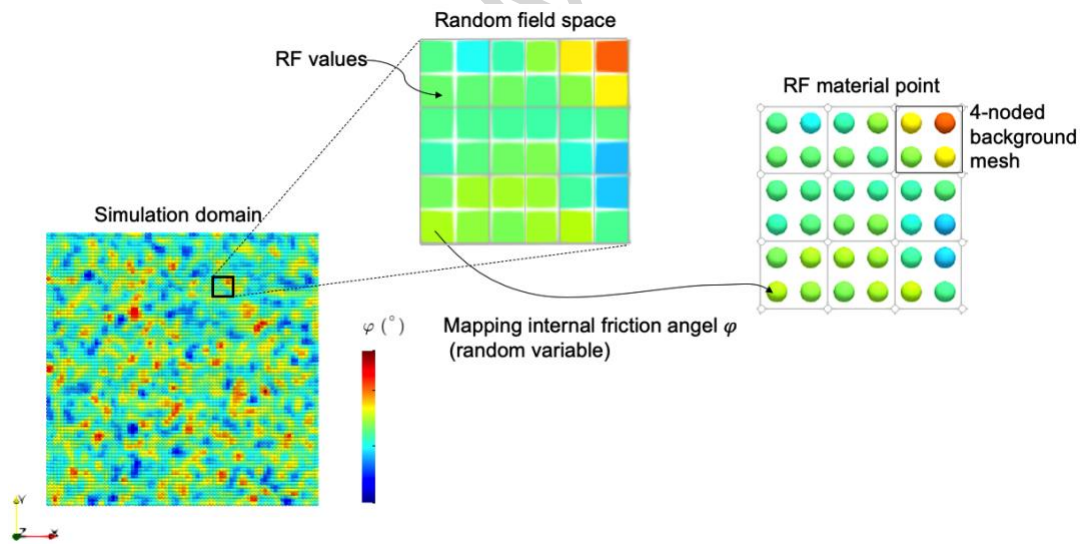


Fig. 5 Schematics of the mapping process of a random field in SGIMP

3. Stochastic analysis of sand column collapse

3.1. Numerical model setup

3.1.1. Deterministic model parameters

The numerical model is setup as a plane strain problem. Fig. 6 shows the initial geometry of the sand column model with 5.0×5.0 m, and the distance from the right side of the sand column to the right-side boundary is 15.0 m for allowing enough runout distance for the sand flow. The computation domain is discretized into 6400 material points with a radius of 0.0625 m (0.625 dm) and covered by a total of 10170 background computational grids with side length of 0.125 mm (1.25 dm). The background computational mesh is made up of 4-noded quadrilateral elements, where each grid contains 4 (2×2) material points inside. The bottom boundary $y = 0$ is fully fixed in the x , y , z directions. While roller boundary conditions are set for allowing vertical displacements at both lateral boundaries ($x = 0$ and $x = 20$ m). On the boundaries of $z = 0$ m and $z = 0.0625$ m, the grid nodes are fixed in the z -direction. Lube et al. (2004) suggested that the roughness of the base surface on which the sand spreads has a negligible effect on the runout distance. This can be explained by the fact that the majority of the actual flow generally occurs over the base of the deposit. Therefore, rough contact, inherent in the MPM, was used in the analysis. The time increment is 2.0×10^{-2} s and total time for the calculation is 5 s when deposits become stable according to kinetic energy and unbalanced forces of the system (Kafaji 2013).

A Mohr-Coulomb model is used to describe the sand behavior, the material properties are summarized in Table 2. To realistically model the post-failure behavior of the sand collapse, a numerical damping is introduced for approximating the energy loss of grains on movement, which is mainly influenced by the effect of friction between particles (Sołowski and Sloan, 2015).

Without such damping factor, the spreads of sand particles can be too far (Sołowski and Sloan, 2013). The numerical damping is applied using:

$$a_I = a_I - c_d v_I \quad (14)$$

where a_I is the acceleration of the nodes on the background grids, v_I is the velocity of nodes on the background grids and c_d is the damping coefficient. In the model, the value of damping coefficient has been selected as 2.

Table 2. Material properties of the sand

Parameters	unit	Values
Bulk density, ρ	kg/m ³	1450
Young's modulus, E	kPa	2600
Poisson's ratio, ν		0.31
Internal friction angle, ϕ	°	35

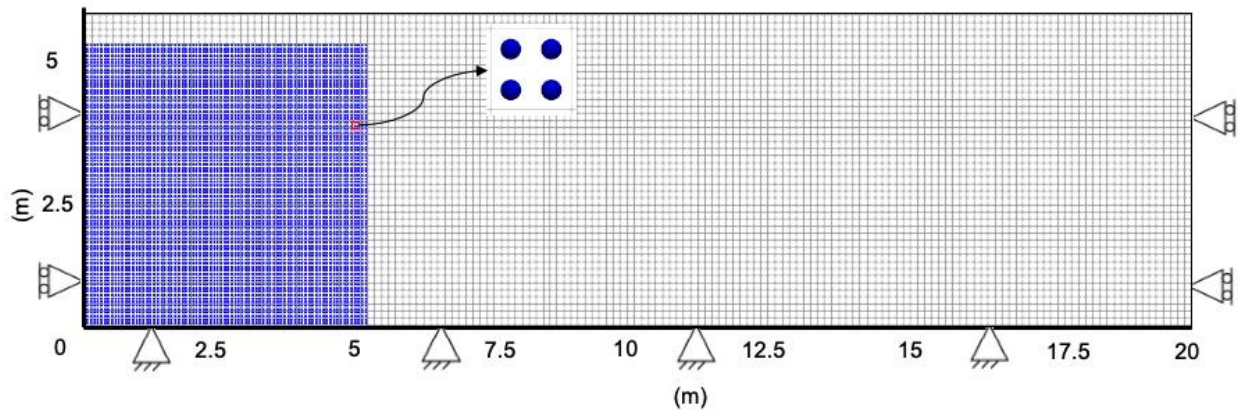


Fig. 6 Geometry and boundary conditions of the model

3.1.2. Stochastic model parameters

Sand is a natural geomaterial with heterogeneities subject to long-term geological processes. Since Lumb (1966, 1970) investigated the natural variability of internal friction angle of sand, many researchers started to build random variable model for sand. It is admitted that even small-scale heterogeneities of internal friction angle φ have strong influence on macroscopic behavior, such as internal structure deformation and flow distances (Hungr, 1995). Therefore, this soil strength parameter is selected as the random variable for the analysis. Different plausible ranges of variations for both $\tan\varphi$ and φ of sand, according to the literature, are summarized in Table 3.

Table 3. General summary of the ranges of the COV reported in the literature for friction angle of sand

Values of COV	PDF	Reference
$\text{COV}_{\tan\varphi} = 0.058$	-	Lumb (1966)
$\text{COV}_{\varphi} = 0.053$	Log-normal distribution	Schultze (1972)
$\text{COV}_{\tan\varphi} = 0.073$		
$0.05 \leq \text{COV}_{\tan\varphi} \leq 0.14$	-	Schultze (1975)
$0.037 \leq \text{COV}_{\varphi} \leq 0.093$	Normal distribution	Wolff et al. (1996)
$0.05 \leq \text{COV}_{\varphi} \leq 0.11$	-	Phoon and Kulhawy (1996)
$0.05 \leq \text{COV}_{\tan\varphi} \leq 0.14$	-	
$0.02 \leq \text{COV}_{\varphi} \leq 0.05$	Normal distribution	Lacasse and Nadim (1997)
$\text{COV}_{\varphi} = 0.059$		
$0.05 \leq \text{COV}_{\tan\varphi} \leq 0.15$	-	Cherubini (2000)
$0.054 \leq \text{COV}_{\tan\varphi} \leq 0.167$	-	Wang et al. (2010)

According to the summary, in this work, the internal friction angles are described by a normal distribution and the statistical characteristics of sand parameters are displayed in Table 4. The

mean value is $\mu_\varphi=35^\circ$ and values of coefficient of variation, COV_φ , equal to 0.05, 0.10, and 0.15, are used to study the effect of degree of heterogeneity on the macroscopic response. Only isotropic random fields with $\delta_h = \delta_v = 0.2 \text{ m}$ are used in this study (usually 0.13 m to 0.71 m), which is based on the CPT cone resistance data reported in the literature (Campanella et al., 1987; Nie et al., 2015).

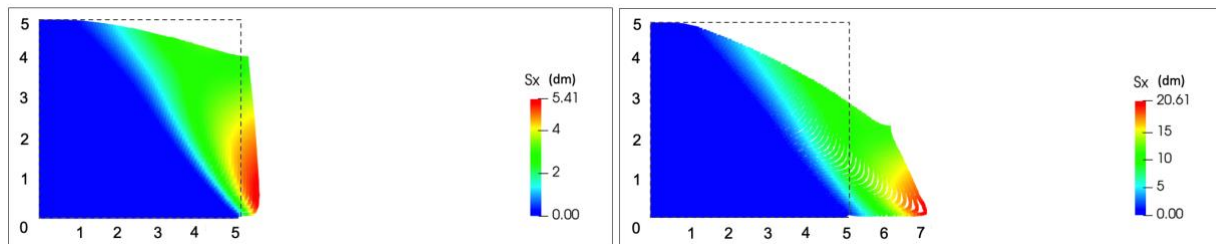
Table 4. Statistical parameters of the internal friction angle φ of sand

Parameters	unit	Values	Distribution
Mean, μ_φ	°	35	Normal distribution
COV_φ	-	0.05, 0.10, 0.15	
Horizontal fluctuation, δ_h	m	0.2	
Vertical fluctuation, δ_v	m	0.2	

4. Numerical modeling

4.1. Homogeneous sand collapse modeling

By conducting the homogeneous sand collapse modeling with constant parameters in Table 2, the runout distance S_x of sand collapse at critical times are presented in Fig. 7. For better visualization of the modeling, the unit is set as decimeter (dm). When $t=1.4 \text{ s}$, the runout distance starts increasing rapidly, and a large deformation can be observed. When $t=4.2 \text{ s}$, the sand collapse is stable, and its final runout distance reaches 60.03 dm.



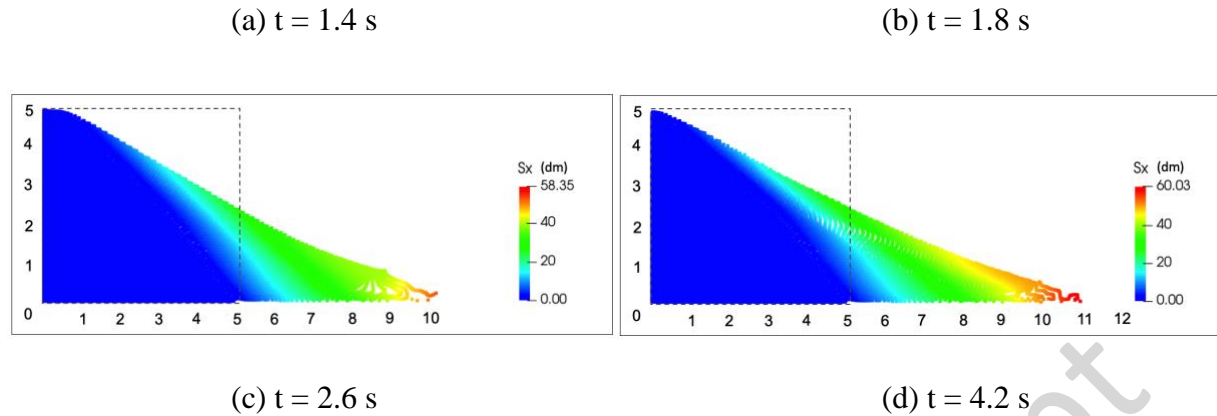


Fig. 7 Homogeneous sand collapse process represented by horizontal runout distance at different times

4.2. Heterogeneous sand collapse modeling

From this section on, a stochastic modeling of sand collapse considering the effect of soil heterogeneity is conducted, in which the five previously introduced ACFs and three different values of COV_{φ} are used to specify the most influential heterogeneous characteristics on the mechanical responses. In these simulations, the baseline case is defined when the COV_{φ} is taken as 0.05, and the horizontal and vertical scale of fluctuations are taken as $\delta_h = \delta_v = 0.2$ m.

Fig. 8 presents the typical samples of random fields of φ with the baseline case parameters associated with the SNX, SQX, SMK, CSX, and BIN ACFs. In these figures, the red regions denote larger φ values representing the mechanically strong zones, while the blue regions represent relatively smaller φ values specifying the mechanically weaker zones in the sand column. All typical samples of random fields show that heterogeneity causes a random distribution of local weakness (low values of φ) in the domains. These weak zones will introduce different final output responses, which cannot be predicted by homogeneous modeling. It can also be observed that the generated random samples associated with SQX and SMK ACFs present relatively smoother

variations among sand friction angle values, hence they provide more realistic representation of the spatially correlated soil strength characteristic (Li et al., 2015). While the SNX, CSX, and BIN ACFs result in generating random samples with higher degrees of fluctuation, where the random values vary quite roughly (as shown in Fig. 8).

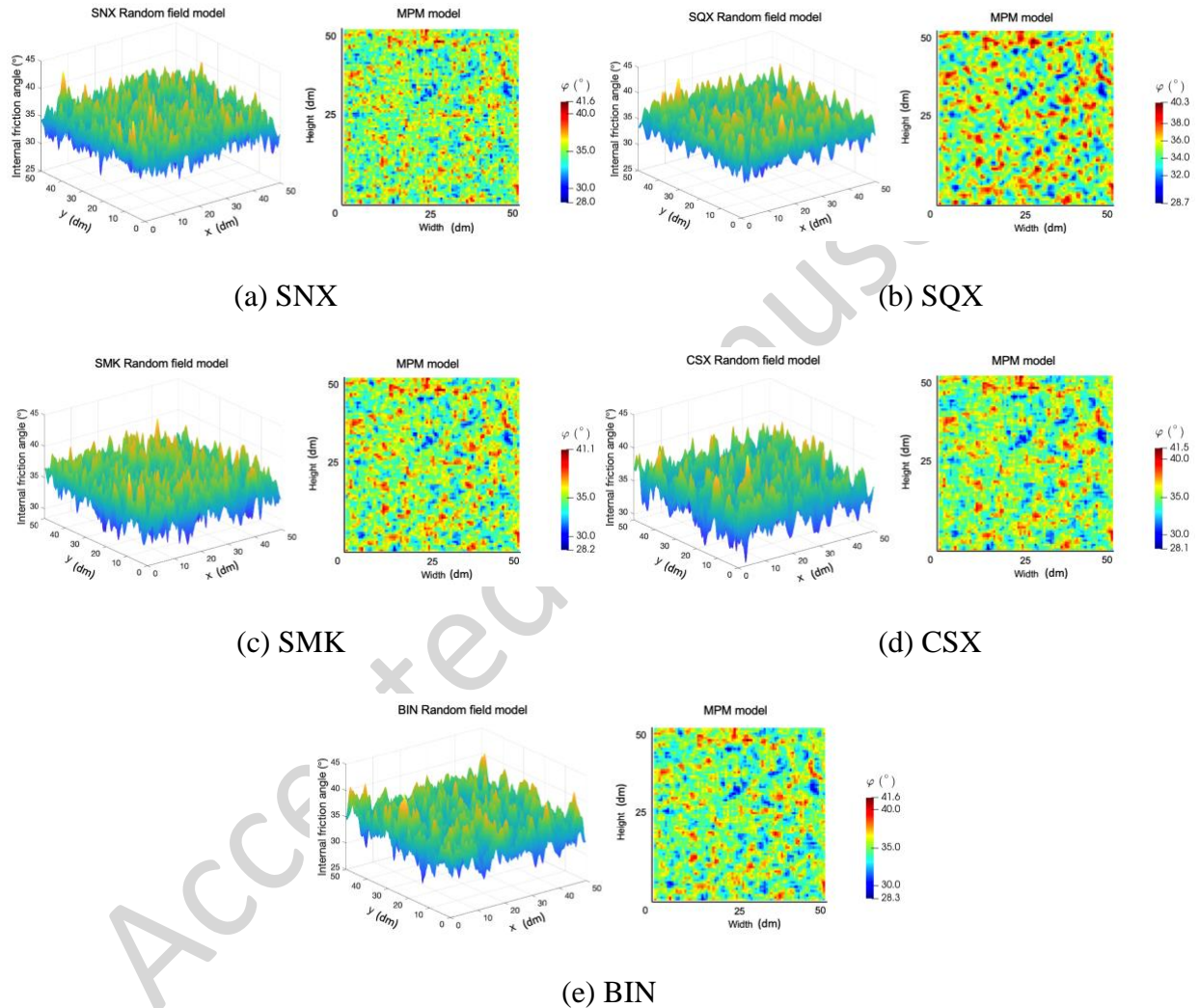


Fig. 8 Typical samples of random fields associated with the ACFs of $COV_{\phi} = 0.05$, $\delta_h = \delta_v = 0.2$ m, red and blue regions depict mechanically “strong” and “weak” sand, respectively.

Fig. 9 shows the collapse status of the heterogeneous sand at final state, predicted by using different ACFs in the SGIMP simulations. With different ACFs, the frontal deposits spread over a range, from about 110 dm to over 120 dm, that demonstrates the impact of considering sand heterogeneity on the modeling results.

To comprehensively analyze the impact of the key mechanical features on the runout distance, the stochastic response of the runout distance S_x is computed using MCS with different ACFs and $COV\phi$ values. The number of samples is crucial for the statistical accuracy. Large numbers would lead to more accurate estimations with lower errors, but they require dramatic computational time. Therefore, an appropriate MCS number is determined by compromising between the efficiency and accuracy. In this work, both the mean values and standard deviations of the S_x for the five ACFs with the baseline cases are plotted as functions of the number of MCS. It demonstrates that after about 700 simulations the statistical convergence is achieved (Fig. 10). Therefore, one thousand realizations are performed for each case to confirm stable statistical results and computational efficiency. Each realization takes about 8 ~ 10 minutes when using a PC with an Intel Core i7-6700 3.40 GHz processor with 8 cores and 16 GB memory.

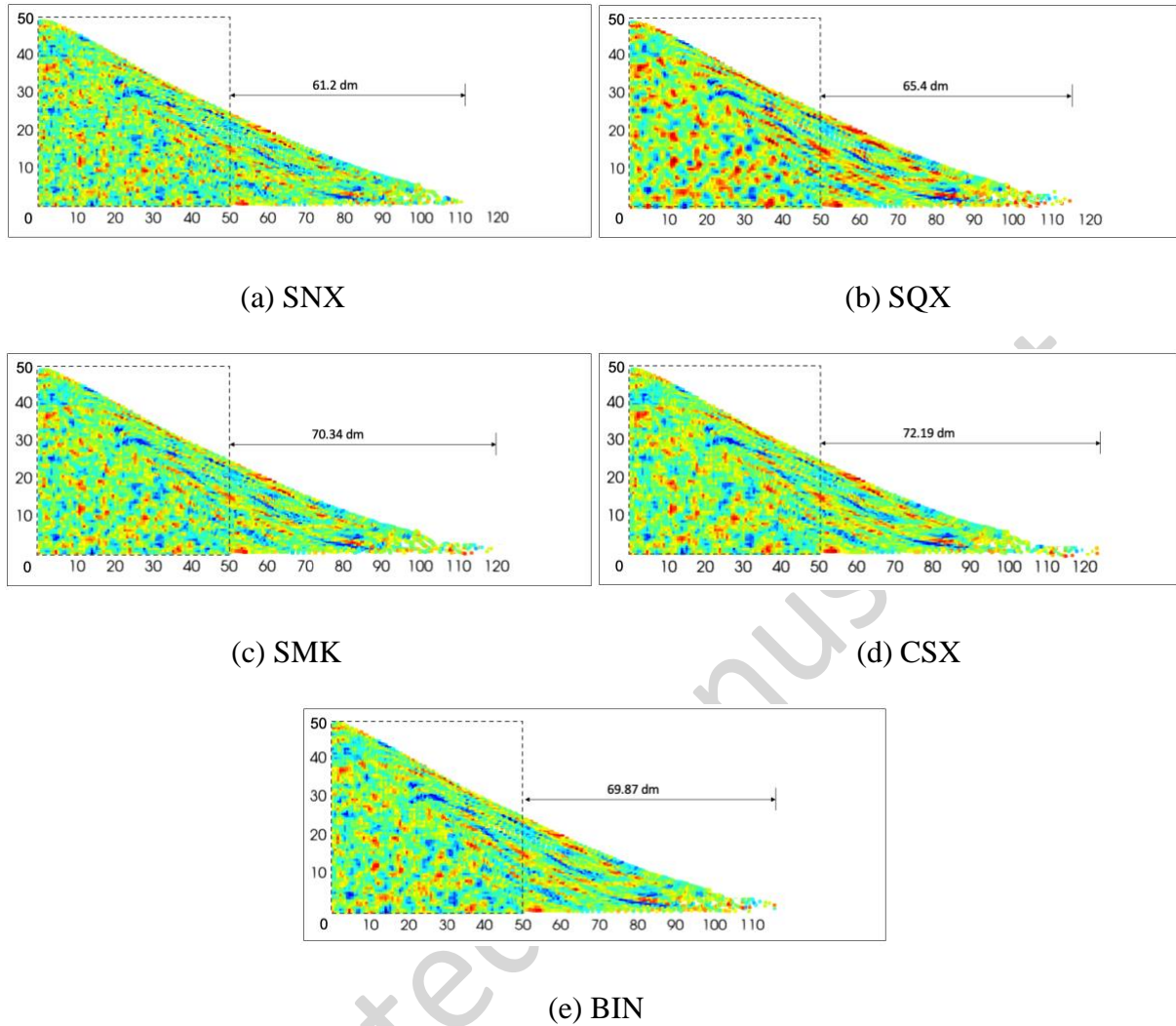


Fig. 9 Final configuration of the heterogeneous sand collapse ($COV_{\varphi} = 0.05$)

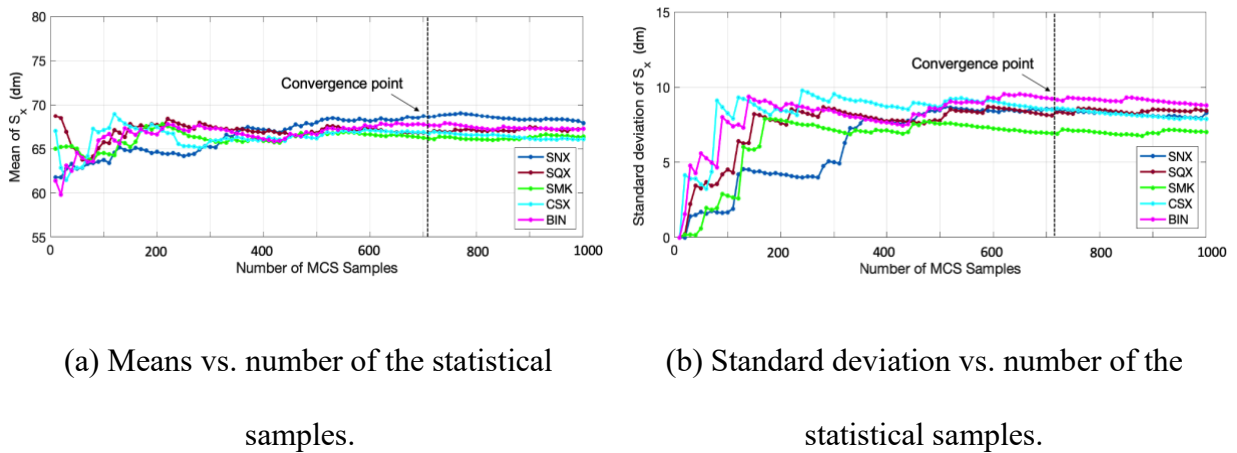


Fig. 10 Variations of the mean and standard deviation of the S_x with the number of MCS samples based on the baseline case.

4.2.1. Effect of ACFs on runout distance

In the previous section, the effects of different ACFs on the runout distance of heterogeneous sand collapse were investigated by the SGIMP analysis in which 1000 samples of friction angle random field were generated and evaluated to obtain an accurate estimation of each case. In order to identify the distribution of the computed runout distance for each case, four different types of statistical distributions including normal distribution, lognormal distribution, Gumbel and Weibull distributions are examined. A goodness-of-fit test method is applied to identify the best-fit marginal distribution underlying the computed data. In this work, both the Akaike information criterion (AIC) (Akaike, 1974) and Bayesian information criterion (BIC) (Schwarz, 1978) are adopted to identify the best-fit distributions, they are defined as

$$AIC = -2 \sum_{i=1}^N \ln f[(x_i; p, q)] + 2k_1 \quad (15)$$

$$BIC = -2 \sum_{i=1}^N \ln f[(x_i; p, q)] + k_1 \ln N \quad (16)$$

where x_i ($i = 1, 2, \dots, N$) is the output S_x from the SGIMP; N is the number of samples; $f(x_i; p, q)$ is the PDF of alternative marginal distribution function, p and q are the parameters of distribution; k_1 is the number of distribution parameters in the alternative marginal distribution. For the above-mentioned marginal distribution function, k_1 is considered to be equal to 2 (Phoon and Ching, 2014; Zhang et. al., 2018).

Table 5 shows the AIC and BIC values associated with the four distributions for various ACF conditions. Note that the distribution associated with the smallest AIC and BIC values is identified to be the best-fit marginal distribution to the output data (Zhang et. al., 2018). It is found that both the AIC and BIC values indicate the Gumbel distribution is the best-fit distribution for the output runout distance of all cases.

Table 5. AIC and BIC values for the candidate distributions

ACF	Normal [AIC, BIC]	Lognormal [AIC, BIC]	Gumbel [AIC, BIC]	Weibull [AIC, BIC]
SNX	702.86, 708.07	693.00, 698.21	676.12, 681.33*	738.54, 743.75
SQX	714.45, 719.66	699.41, 704.62	676.15, 681.36*	767.03, 772.24
SMK	677.71, 682.92	665.38, 670.59	642.25, 647.46*	741.22, 746.43
CSX	688.59, 693.80	675.25, 680.46	652.28, 657.49*	751.64, 756.85
BIN	722.87, 728.08	708.45, 713.66	687.49, 692.70*	768.87, 774.08

*Denotes the minimum AIC and BIC values, which correspond to the best-fit distributions.

The PDF of the Gumbel distribution is expressed as (Phoon and Ching, 2014):

$$f(x; p, q) = \frac{q \exp\{-q(x - p) - \exp[-q(x - p)]\}}{\{1 - \exp[-\exp(pq)]\}} \quad (17)$$

$$\mu = p + 0.5772/q \quad (18)$$

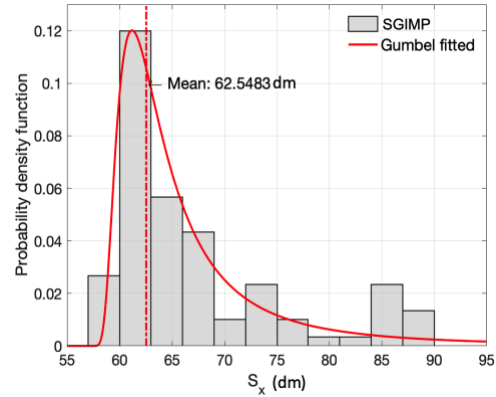
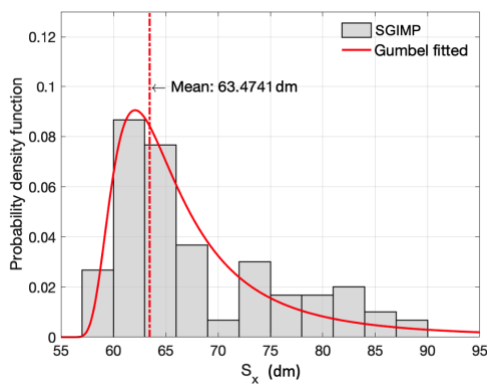
$$\sigma^2 = \pi^2/(6q^2) \quad (19)$$

where p and q are the parameters of distribution, μ is the mean value, and σ is the standard deviation. In this work, maximum likelihood method is adopted to estimate the corresponding parameters of the Gumbel distribution. The mean and deviation of stochastic data can be obtained by equations (17-19).

Fig. 11 shows the distributions and mean values of runout distance S_x of each heterogeneous sand collapse case associated with different ACFs. It should be noted that the probabilistic post-failure behavior analysis is different from the pre-failure analysis such as stability analysis or reliability analysis. The effect of ACFs on runout distance shows different features compared with other works (e.g., stability or reliability analysis of slopes (Li et al. 2015; Ching and Phoon 2019)). Because of the diverse spatial distribution of friction angle generated by different ACFs, each output runout distance is different. The runout distances predicted by the heterogeneous models range from 57 dm to 89 dm. By comparing the mean values, the results of SNX with a value of 63.47 dm are larger than those obtained by the other ACFs. While the results of SQX and SMK are very close to each other with 62.54 dm and 62.65 dm, respectively. The results achieved by CSX and BIN are relatively smaller than the other cases, with 62.35 dm and 62.37 dm, respectively. The relative difference in mean value of the runout distance associated with these ACFs can be explained by their function graphs and expressions. According to Fig. 3, a sharp decrease can be observed in the SNX surface, which suggests that the random internal friction angle based on SNX spatially fluctuates significantly, thus predicting larger values for the runout distance. As for other ACFs, the surfaces are relatively smooth, presenting more realistic variations than those of the SNX ACF, which result in more reliable predictions. This is consistent with the previous findings of Uzielli et al. (2005) that SMK and CSX are suitable for characterizing the spatial correlation of shear strength of sands.

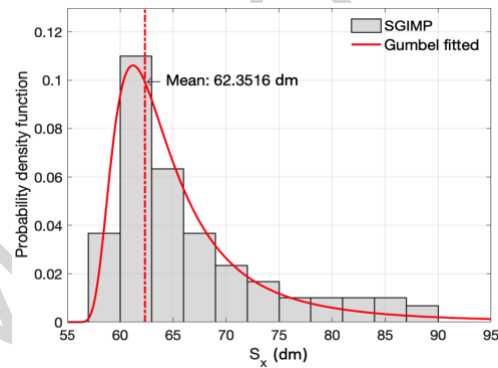
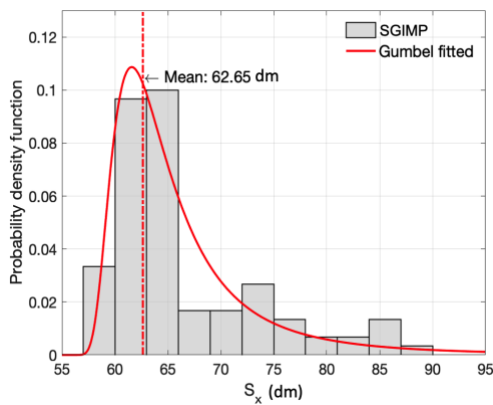
In Fig. 12, it can be observed that the effect of ACFs on runout motion of sand collapse are slightly different, in which SNX shows the largest impact on post-failure behavior of flows among the different ACF cases. Additionally, the homogeneous model underestimates the runout distance with only 60.03 dm, which is apparently because the effect of local spatial variation in the friction

angle is not considered in the deterministic analysis. A recognizable difference can be noticed in terms of ϕ of the sand. In addition, between 55% to 68% of the runout distances predicted by the heterogeneous models with all cases exceeding the runout distance obtained by the deterministic model, which means there is a large uncertainty in prediction of the runout distances. Because flow of the granular materials depends on the interparticle frictions (Crosta et al., 2009), the spatial variation of ϕ would significantly influence the post-failure behavior. Therefore, the homogeneous model cannot reproduce the aspect of the post-failure behavior of the heterogeneous sand collapse and as such it cannot predict the real post-failure behavior and the runout distance of the sand collapse.



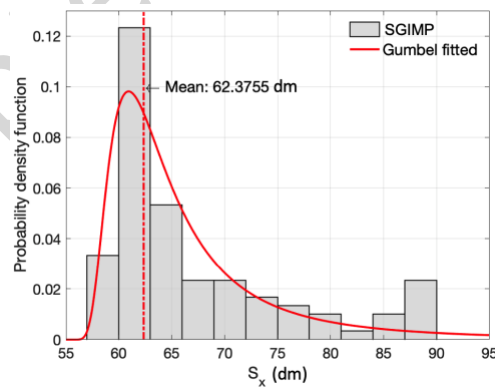
(a) SNX

(b) SQX



(c) SMK

(d) CSX



(e) BIN

Fig. 11 Histograms, PDF and mean values of S_x with the ACF cases

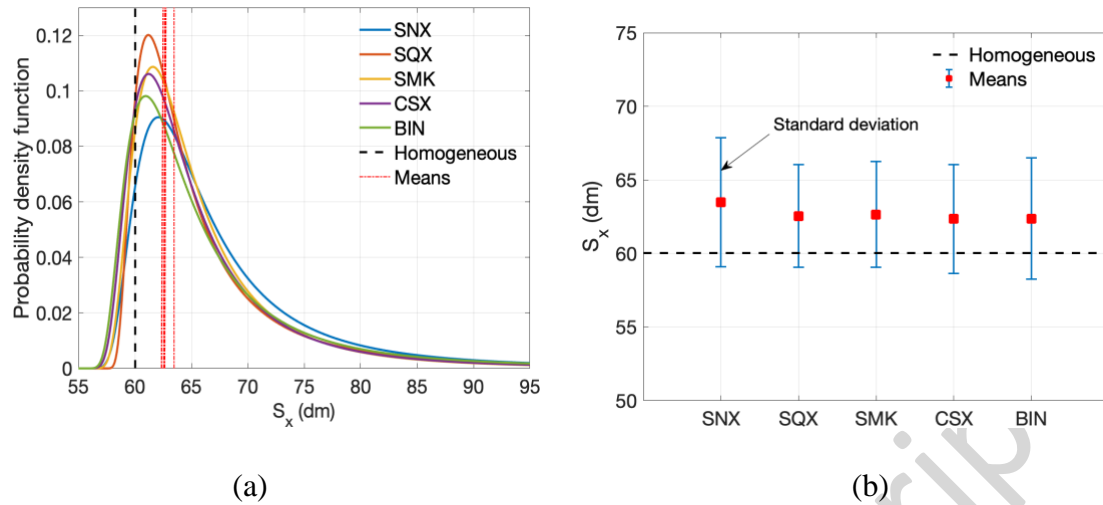
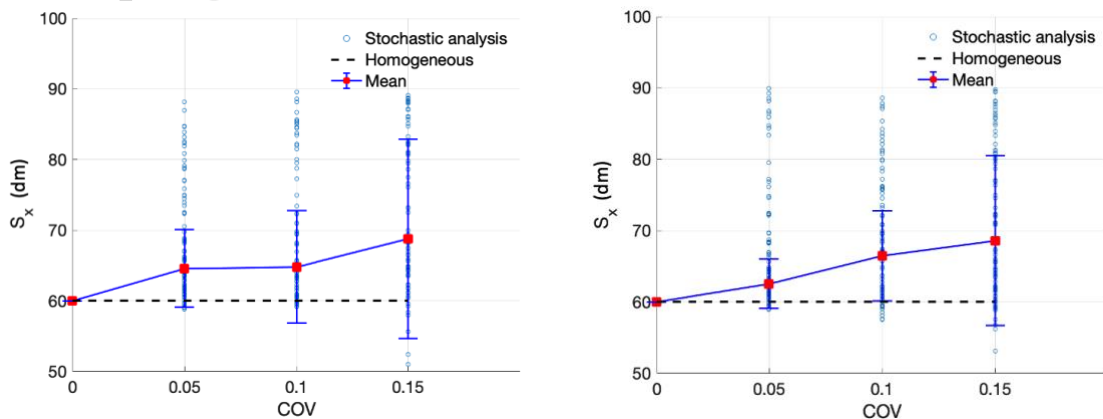


Fig. 12 (a) PDFs with the ACFs compared with homogenous results, (b) Mean values and standard deviations of S_x with the ACFs.

4.2.2. Effect of COV_ϕ on runout distance

To investigate the effect of COV_ϕ on the runout distance of the heterogeneous sand collapse, the COV_ϕ is increased from 0.05 to 0.15 with constant $\delta_h = \delta_v = 0.2$ m in each ACF case. A total of 5000 simulations have been conducted. According to the statistics, the mean values and standard deviations of the runout distance in each case (considering different COV_ϕ values) are plotted in Fig. 13, and compared with the runout distances predicted by the deterministic analysis.



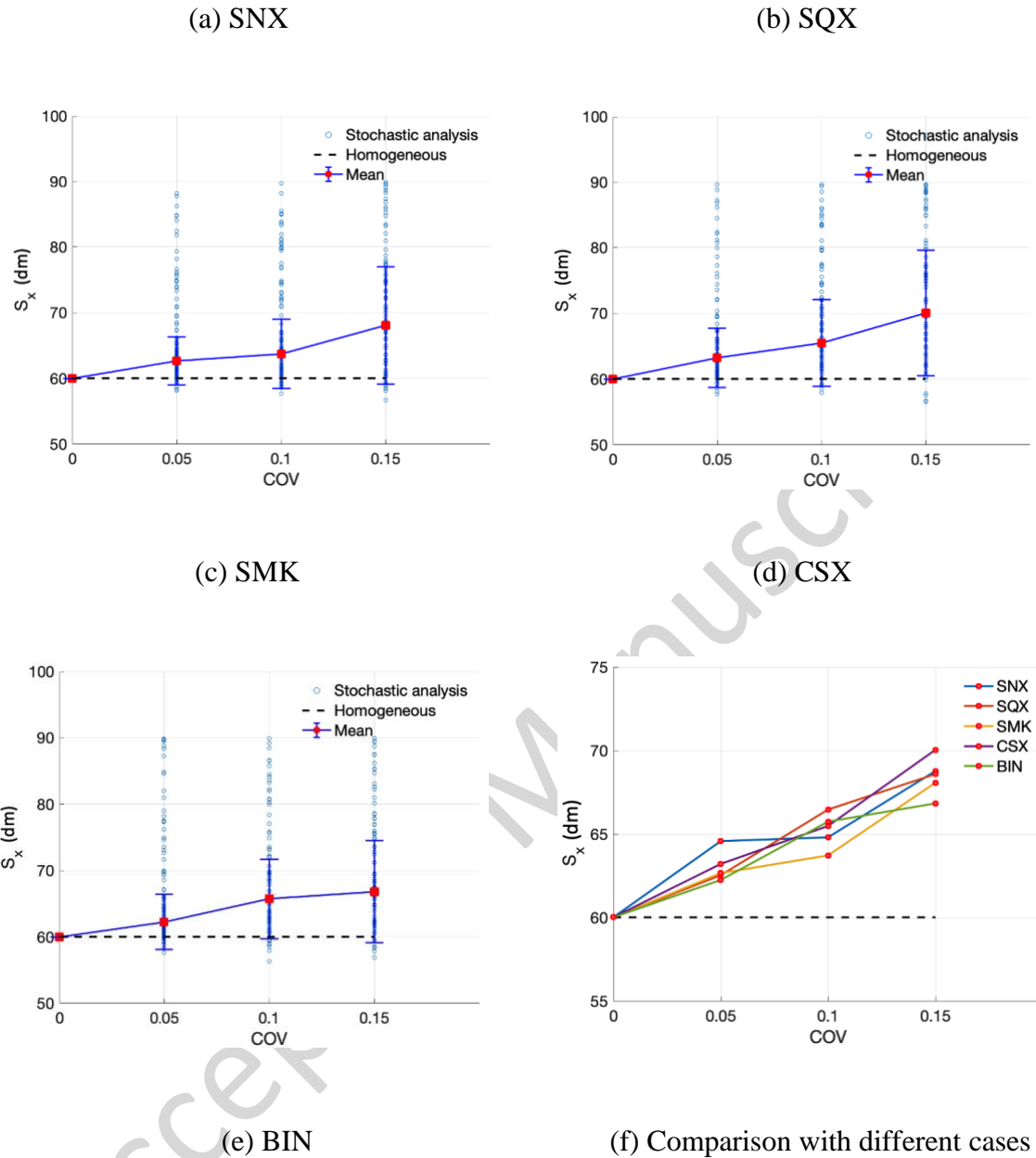


Fig. 13 Mean values and standard deviations of the runout distances considering different COV_φ

All results show that the mean values of the runout distance increase with increasing COV_φ , and all the mean values are larger than the value obtained from the homogeneous model. Additionally, the number of the extreme values of the runout distance increases with the COV_φ increase. For a small COV_φ , the varying range of φ is correspondingly narrowed. Thereby, the distribution of the

runout distances will be narrower. On the other hand, a large COV_{φ} causes a wide range of values for φ , subsequently resulting in a wider distribution of the runout distance. Therefore, the standard deviations of the runout distance become large with the increase in COV_{φ} value.

Fig. 14 shows the exceedance probability of the predicted runout distances (S_x) by all heterogeneous cases that larger runout distance is obtained compared to that of the deterministic analysis. It shows that the uncertainty in predicting the S_x is significantly enlarged as COV_{φ} increases. Moreover, it is found that different ACFs have relatively different effects on the S_x outputs when COV_{φ} is increasing, but the overall trends are similar with each other. As for SMK, the result with $COV_{\varphi}=0.05$ illustrates that only 39% of the predicted cases exceed the deterministic value, which indicates that the smallest uncertainty on S_x is when using SMK. While the results with $COV_{\varphi}=0.15$, generating from CSX, demonstrate the largest uncertainty in predicting the runout distance, as 74% of the outputs exceed the deterministic value. All probabilities of the runout distance exceed the value obtained by the homogeneous model, indicating that sand heterogeneity significantly influences on the magnitude of the runout distance and post-failure behavior. It also indicates that potentially longer runout distance can be caused by the increasing of COV_{φ} .

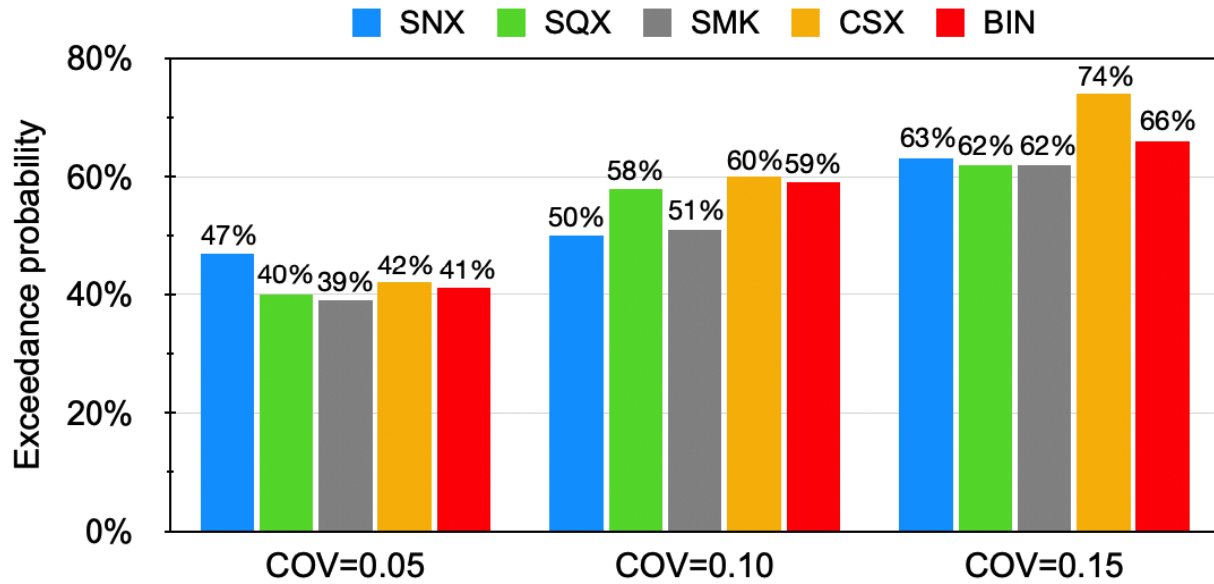


Fig. 14 Probability of S_x exceeding the deterministically predicted value in each case

5. Conclusion

A SGIMP framework is proposed for probabilistic analysis of runout distance in sand collapse considering the heterogeneity of soil shear strength. The framework is based on the integration of random fields theory and GIMP into a Monte-Carlo simulation basis. Heterogeneity and large deformation are both considered in this method, and the capability of the SGIMP framework to estimate the runout distance of heterogeneous sand collapse has been explored, through which the effects of different ACFs and COV on the runout distance have also been investigated. The main findings of the study are summarized in the following:

1. The proposed SGIMP framework can be used to generate reasonable random fields for stochastic large-deformation failure analysis, and it provides a practical tool for solving large deformation problems in deposits with prominent heterogeneity.

2. Using the proposed framework, a heterogeneous sand collapse is simulated with both homogeneous and heterogeneous conditions. The results show that the homogeneous model may underestimate the runout distance while the stochastic-based analysis provides more realistic results. Due to the differences of adopted ACFs, the runout distance outputs associated with different ACFs are dissimilar. Among the five ACFs, it is shown that SNX results in the largest possible post-failure material flow with apparent overestimation of runout distances. As for other ACFs, more realistic variations of soil strength parameter are obtained which result in more reliable predictions. In particular, SMK and CSX seem to be the most suitable for characterizing the spatial correlation of shear strengths.

3. The COV_{ϕ} affects the runout distance of sand collapse. The uncertainty of runout distance increases with COV_{ϕ} increasing, accordingly the distribution of the runout distance also increases, which indicates that the deviations of the runout distance become larger.

4. According to the proportion of the runout distance that exceeds the deterministic value in each case, the results imply that a deterministic analysis would significantly underestimate the potential risk caused by the large runout distance induced by heterogeneous sand collapse.

As has been clarified, the main focus of this paper was to study the implications of using different ACFs on stochastic analysis of post-failure runouts due to sand collapse within a SGIMP framework. However, it should be mentioned that, within this framework, there are other factors or considerations worth investigating in future works, for example the natural non-stationary characteristics of soil properties (e.g., Ma et al. 2022) or employing more advanced material models (e.g., Wang et al. 2020).

Acknowledgements

The financial support by the European Commission's RFCS project MINRESCUE (Contract RFCS-RPJ-899518), and the National Natural Science Foundation of China Project (Contract: 52150610492) are gratefully acknowledged. The first author would like to acknowledge the support from the Chinese Scholarship Council (CSC) and University of Warwick.

Reference

- Akaike, H. 1974. "A new look at the statistical model identification." *IEEE transactions on automatic control* 19(6):716–723.
- Andersen, S., and L. Andersen. 2010. "Modelling of landslides with the material-point method." *Comput. Geosci.* 14: 137–147.
- Bardenhagen, S. G. 2002. "Energy conservation error in the material point method for solid mechanics." *J. Comput. Phys.* 180 (1): 383-403.
- Bardenhagen, S. G., and E. M. Kober. 2004. "The generalized interpolation material point method." *C. Comput. Model. Eng. Sci.* 5: 477-495.
- Bardenhagen, S. G., J. U. Brackbill, and D. Sulsky. 2000. "The material-point method for granular materials." *Comput. Methods in Appl. Mech. Eng.* 187(3-4):529–541.
- Benvenuti, L., C. Kloss, and S. Pirker. 2016. "Identification of DEM simulation parameters by Artificial Neural Networks and bulk experiments." *Powder technol.* 291:456-465.
- Bui, H. H., R. Fukagawa, K. Sako, and S. Ohno. 2008. "Lagrangian meshfree particles method (SPH) for large deformation and failure flows of geomaterial using elastic-plastic soil constitutive model." *Int. J. Numer. Anal. Methods. Geomech.* 32(12):1537–1570.
- Cafaro, F., and C. Cherubini. 2002. "Large sample spacing in evaluation of vertical strength

- 562 variability of clayey soil.” *J. Geotech. Geoenvironmental. Eng.* 128(7):558–568.
- 563 Campanella, R. G., D. S. Wickremesinghe, and P. K. Robertson. 1987. “Statistical treatment of
564 cone penetrometer test data.” *Proceedings of the 5th International Conference on
565 Application of Statistics and Probability*, Rotterdam. 1011-1019.
- 566 Cherubini, C. 2000. “Reliability evaluation of shallow foundation bearing capacity on $c'\phi'$ soils.”
567 *Can. Geotech. J.* 37(1):264–269.
- 568 Ching, J. and K.K. Phoon. 2019. “Impact of autocorrelation function model on the probability of
569 failure.” *J. Eng. Mec.* 145(1):04018123.
- 570 Ching, J., K. K. Phoon, A. W. Stuedlein, M. Jaksa. 2019. “Identification of sample path smoothness
571 in soil spatial variability.” *Struct. Saf.* 81:101870
- 572 Crosta, G.B., S. Imposimato, and Roddeman, D., 2009. Numerical modeling of 2-D granular step
573 collapse on erodible and nonerodible surface. *J. Geophys. Res. Earth Surf.* 114(F3).
- 574 DeGroot, D. J., and G. B. Baecher. 1993. “Estimating autocovariance of in-situ soil properties”. *J.*
575 *Geotech. Eng.* 119(1):147-166.
- 576 Fenton, G. A., and D. V. Griffiths. 2003. “Bearing-capacity prediction of spatially random $c\phi$
577 soils.” *Can. Geotech. J.* 40(1):54–65.
- 578 Fern, E. J., and K. Soga. 2017. “Granular column collapse of wet sand.” *Procedia Eng.* 175:14–20.
- 579 Gironacci, E., M. M. Nezhad, M. Rezaia, G. A. Lancioni. 2018. “Non-local probabilistic method
580 for modeling of crack propagation.” *Int. J. Mech. Sci.* 144:897–908.
- 581 Griffiths, D. V., and G. A. Fenton. 2004. “Probabilistic Slope Stability Analysis by Finite
582 Elements.” *J. Geotech. Geoenvironmental. Eng.* 130:507–518.
- 583 Guo, Y., and J. S. Curtis. 2015. “Discrete element method simulations for complex granular flows.”
584 *Annu. Rev. Fluid Mech.* 47:21–46.

- 585 Huang, J., and D. V. Griffiths. 2015. "Determining an appropriate finite element size for modelling
586 the strength of undrained random 408 soils." *Comput. Geotech.* 69:506–513.
- 587 Huang, L., S. Huang, Y. Liang. 2018. "Probabilistic Settlement Analysis of Granular Soft Soil
588 Foundation in Southern China Considering Spatial Variability." *Granularity in Materials*
589 *Science*, 25.
- 590 Huang, R., and X. Fan. 2013. "The landslide story." *Nat. Geosci.* 6:325–6.
- 591 Hungr, O. 1995. "A model for the runout analysis of rapid flow slides, debris flows, and
592 avalanches." *Can. Geotech. J.* 32(4):610–623.
- 593 Iaconeta, I., A. Larese, R. Rossi, and Z. Guo. 2017. "Comparison of a material point method and a
594 galerkin meshfree method for the simulation of cohesive-frictional materials." *Materials*.
595 10(10):1150.
- 596 Jiang, S. H., D. Q. Li, L. M. Zhang, C. B. Zhou. 2014. "Slope reliability analysis considering
597 spatially variable shear strength parameters using a non-intrusive stochastic finite element
598 method." *Eng. Geol.* 168:120–128.
- 599 Kafaji, I. K. J. 2013. "Formulation of a Dynamic Material Point Method (MPM) for Geomechanical
600 Problems" Ph.D thesis. Germany: University of Stuttgart.
- 601 Kerswell, R. R. 2005. "Dam break with Coulomb friction: A model for granular slumping." *Phys.*
602 *fluids.* 17(5):057101.
- 603 Lacasse, S., F. Nadim. 1997. "Uncertainties in characterising soil properties." *Publ-NGI.* 201:49-
604 75.
- 605 Lajeunesse, E., A. Mangeney-Castelnau, J. P. Vilotte. 2004. "Spreading of a granular mass on a
606 horizontal plane." *Phys. fluids.* 16(7):2371–2381.
- 607 Li, D. Q., S. Jiang, Z. Cao, W. Zhou, C. Zhou, L. Zhang. 2015. "A multiple response-surface

- 608 method for slope reliability analysis considering spatial variability of soil properties.” *Eng.*
609 *Geol.* 187:60–72.
- 610 Li, X., Y. Xie and M. Gutierrez. 2018. “A soft–rigid contact model of MPM for granular flow
611 impact on retaining structures.” *Comput. Part. Mech.* 5(4):529–537.
- 612 Liu, L. L. 2018. “Efficient and conditional reliability analysis of slopes in spatially variable soils.”
613 Ph.D. thesis, China: The Hong Kong Polytechnic University.
- 614 Liu, L. L., Y. M. Cheng, S. H. Jiang, S. H. Zhang, X. M. Wang, Z. H. Wu. 2017. “Effects of spatial
615 autocorrelation structure of permeability on seepage through an embankment on a soil
616 foundation.” *Comput. Geotech.* 87:62–75.
- 617 Llano-Serna, M. A., M. M. Farias, D. M. Pedroso. 2016. “An assessment of the material point
618 method for modelling large scale run-out processes in landslides.” *Landslides* 13:1057–
619 1066.
- 620 Lube, G., H. E. Huppert, R. S. J. Sparks, M. A. Hallworth. 2004. “Axisymmetric collapses of
621 granular columns.” *J. Fluid Mech.* 508:175.
- 622 Lumb, P. 1966. “The variability of natural soils.” *Can. Geotech. J.* 3(2):74–97.
- 623 Lumb, P. 1970. “Safety factors and the probability distribution of soil strength.” *Can. Geotech. J.*
624 7(3):225–242.
- 625 Ma, G., M. Rezaia, M. M. Nezhad. 2022. “Probabilistic post-failure analysis of landslides using
626 stochastic material point method with non-stationary random fields.” *In 20th International*
627 *Conference on Soil Mechanics and Geotechnical Engineering (ICSMGE 2022)*. Sydney.
628 2022.
- 629 Ma, G., X. Hu, Y. Yin, G. Luo, Y. Pan. 2018. “Failure mechanisms and development of catastrophic
630 rockslides triggered by precipitation and open-pit mining in Emei, Sichuan, China.”

- 631 *Landslides* 15:1401–1414.
- 632 Masoudian, M. S., A. M. A. Hashemi, A. Tasalloti, A. M. Marshall. 2019. “A general framework
633 for coupled hydro-mechanical modelling of rainfall-induced instability in unsaturated
634 slopes with multivariate random fields.” *Comput. Geotech.* 115:103162.
- 635 Morris, J. P. 1996. “Analysis of smoothed particle hydrodynamics with applications.” Ph.D thesis.
636 Australia: Monash University Australia.
- 637 Nezhad, M.M., A.A. Javadi, M. Rezania. 2011. “Modeling of contaminant transport in soils
638 considering the effects of micro- and macro-heterogeneity”. *Hydrology* 404: 332-338.
- 639 Nezhad. M. M. 2010. “Stochastic Finite Element Modelling of Flow and Solute Transport in Dual
640 Domain System” Ph.D thesis. United Kingdom: University of Exeter.
- 641 Nezhad. M. M., E. Gironacci, M. Rezania, N. Khalili. 2018. “Stochastic modelling of crack
642 propagation in materials with random properties using isometric mapping for
643 dimensionality reduction of nonlinear data sets.” *Int. J. Numer. Methods. Eng.* 113:656–
644 680.
- 645 Nguyen, C.T., H. H. Bui, G.D. Nguyen R. Fukagawa. 2017. “A new SPH-based approach to
646 simulation of granular flows using viscous damping and stress regularisation.” *Landslides*
647 14(1):69–81.
- 648 Nie, X., H. Huang, Z. Liu, and S. Lacasse. 2015. “Scale of fluctuation for geotechnical probabilistic
649 analysis.” *Geotech. Saf. and Ris. V* 834-840.
- 650 Phoon, K. K., and J. Ching. 2014. “Risk and reliability in geotechnical engineering.” CRC Press.
- 651 Phoon, K. K., F. H. Kulhawy. 1996. “On quantifying inherent soil variability.” *Geotech. Spec. Publ.*
652 58:326-340.
- 653 Phoon, K. K., S. T. Quek, and P. An. 2003. “Identification of statistically homogeneous soil layers

- 654 using modified Bartlett statistics.” *J. Geotech. Geoenviron. Eng.* 129(7):649–659.
- 655 Schultze, E. 1972. “Frequency distributions and correlations of soil properties. Statistics and
656 Probability in Civil Engineering,” Hong Kong University Press, distributed by Oxford
657 University Press, London.
- 658 Schultze, E. 1975. “Some aspects concerning the application of statistics and probability to
659 foundation structures.” Pages 15–18 of: *Proceeding of the 2nd International Conference on*
660 *the Applications of Statistics and Probability in Soil and Structure Engineering*, Aachen,
661 Germany.
- 662 Schwarz, G. 1978. “Estimating the dimension of a model.” *The annals of statistics*. 461-464.
- 663 Sołowski, W. T., and S. W. Sloan. 2013. “Modelling of sand column collapse with material point
664 method.” Pages 698–705 of: *Proceedings of the 3rd international symposium on*
665 *computational geomechanics (ComGeo III)*.
- 666 Sołowski, W. T., and S. W. Sloan. 2015. “Evaluation of material point method for use in
667 geotechnics.” *Int. J. Numer. Anal. Methods. Geomech.* 39(7):685–701.
- 668 Sulsky, D., Z. Chen, H. L. Schreyer. 1994. “A particle method for history-dependent materials.”
669 *Comput. Methods. Appl. Mech. Eng.* 118:179–196.
- 670 Uzielli, M., G. Vannucchi, and K. K. Phoon. 2005. “Random field characterisation of stress-
671 nomalised cone penetration testing 486 parameters.” *Geotechnique* 55(1):3–20.
- 672 Vanmarcke, E. H. 1977. “Probabilistic Modeling of Soil Profiles.” *J. Geotech. Eng. Div.* 103:1227–
673 46.
- 674 Wang, M., G. Ma, F. Wang. 2020. “Numerically investigation on blast-induced wave propagation
675 in catastrophic large-scale bedding rockslide.” *Landslides* 18:785-791.
- 676 Wang, X., Y. Qiu, S. Slattery, Y. Fang, M. Li, S. Zhu, Y. Zhu, M. Tang, D. Manocha, and C. Jiang.

2020. “A massively parallel and scalable multi-GPU material point method.” *ACM Transactions on Graphics (TOG)* 39, no. 4 (2020): 30-1.
- Wang, Y, S. K. Au, and Z. Cao. 2010. “Bayesian approach for probabilistic characterization of sand friction angles.” *Eng. Geol.* 114(3-4):354–363.
- Wolff, T. F, E. C. Demsky, J. Schauer, E. Perry. 1996. “Reliability assessment of dike and levee embankments.” Pages 636–650 of: *Uncertainty in the geologic environment: From theory to practice*.
- Yerro, A., K. Soga, J. Bray. 2019. “Runout evaluation of Oso landslide with the material point method.” *Can. Geotech. J.* 56(9):1304–1317.
- Zhang, L., J. Li, X. Li, J. Zhang, H. Zhu. 2018. “Rainfall-induced soil slope failure: Stability analysis and probabilistic assessment.” CRC Press.
- Zhang, W and D. Xiao. 2019. “Numerical analysis of the effect of strength parameters on the large-deformation flow process of earthquake-induced landslides.” *Eng. Geol.* 260:105239.
- Zhang, X., Z. Chen, Y. Liu. 2016. “The Material Point Method: a continuum-based particle method for extreme loading cases.” Academic Press.
- Zhu, H., L. Zhang, T. Xiao, Y. Li. 2017. “Generation of multivariate cross-correlated geotechnical random fields.” *Comput. Geotech.* 86:95–107.